Chapter 4
AVO Modeling Results

4.1 Zoeppritz-equations AVO modeling results

The Zoeppritz equations solve the angle-dependent reflectivity problem accurately with given P-wave velocity, S-wave velocity, and density for a single boundary half-space model. Because the equations are so complex and need a computer program to be solved, I used a program developed by Youn (1998) that utilizes the computer subroutine by Young and Braile (1976). However, the basic assumptions in the Zoeppritz equations that are isotropic media and plane-wave theory, constrain the real accuracy of AVO modeling results. It is well known that anisotropy in shale could affect AVO rather significantly. Also a source wavefield in exploration seismology is spherical rather than planar inducing interference effects in AVO.

All the picked lithologic units at Well C have gone through the full Zoeppritz-equations AVO modeling using the elastic parameters (picked from well logs) shown in Table 2.3. Figures 4.1 and 4.2 show the modeling results. The three gas sands show somewhat typical class-III-type AVO (Rutherford and Williams, 1989). The gas sands 2 and 3 show relatively strong positive AVO trend (the magnitude of amplitude increases with offset) and gas sand 1 relatively weak (Figure 4.1-a). The significant increases in S-wave velocities of the gas sands over the overlying shale cause this positive AVO trend, while the lower P-wave velocity and density of the sands than those of shale cause negative zero-offset reflectivity.

The four wet sands show an almost flat AVO trend with relatively medium to strong amplitude levels (Figure 4.1-b). The wet sands 2 and 3 show a slightly negative AVO trend (the magnitude of amplitude decreases with offset). The wet sand 4 shows a slightly positive AVO trend. The wet sand 1 shows a flat AVO trend. The slight increases or decreases in S-wave velocities of the wet sands over the overlying shale cause this flat AVO trend with slight variations.

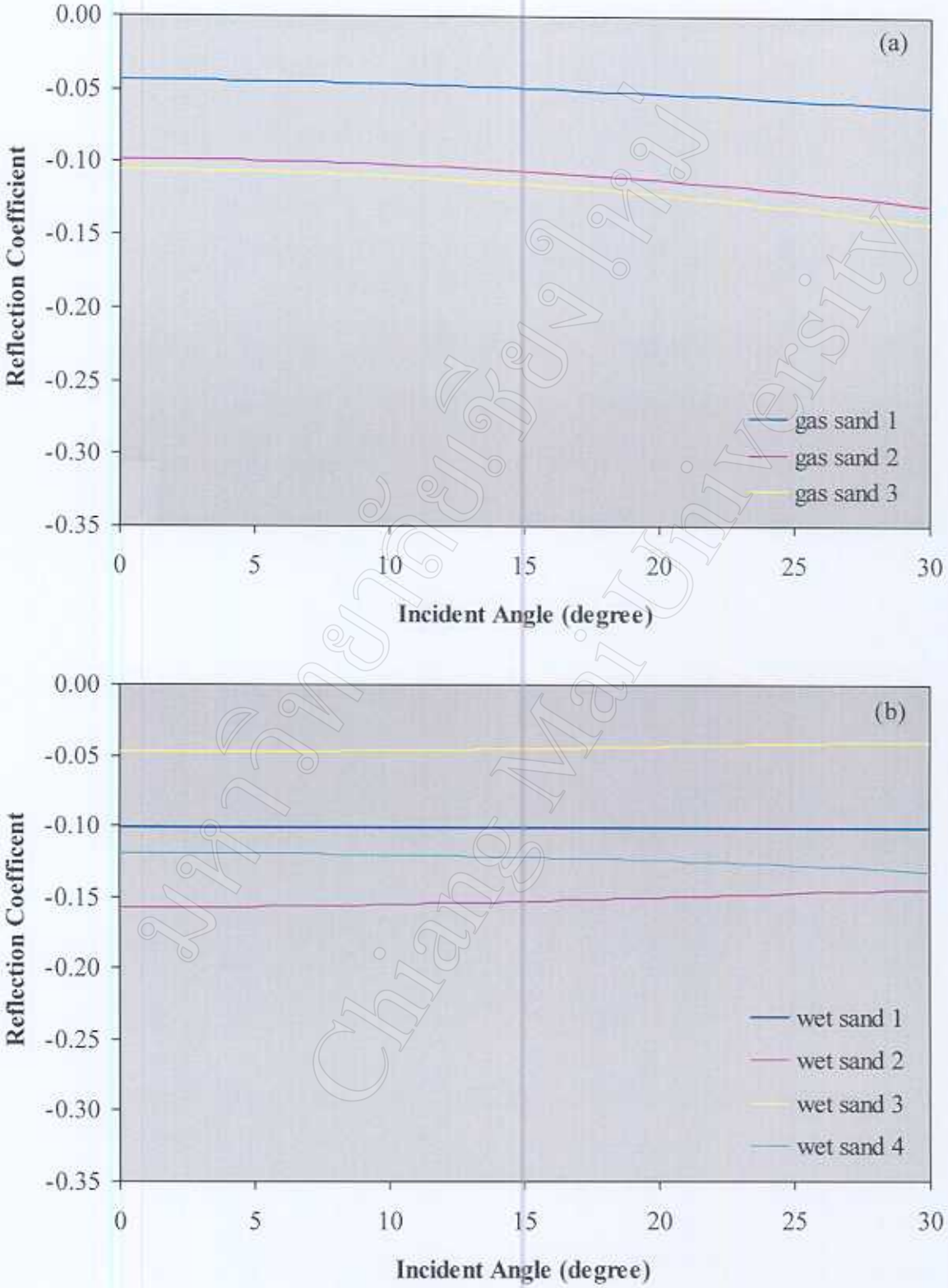

Figure 4.1 Incident angle and reflection coefficient relationships for (a) the three gas sands and (b) the four wet sands.

มหาวิทยาลัยเชียงใหม่ Chiang Mai University

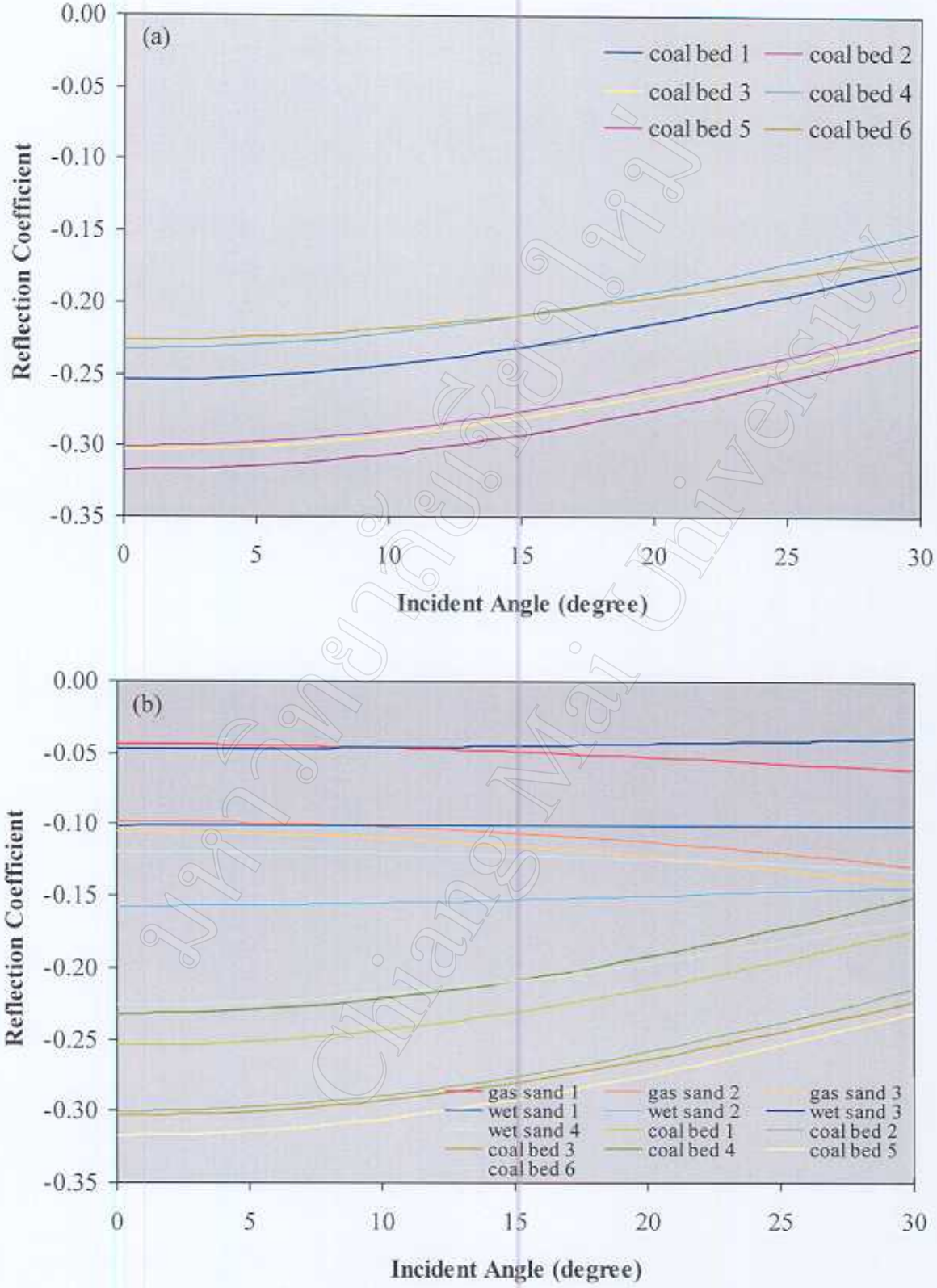

Figure 4.2 Incident angle and reflection coefficient relationships for (a) the six coal beds (b) all the gas sands, wet sands, and coal beds.

มหาวิทยาลัยเชียงใหม่ Chiang Mai University

The six coal beds show a strong negative AVO trend with strong negative zero-offset amplitudes (Figure 4.2-a). All the coal beds are characterized by low P-wave velocity, S-wave velocity, and density relative to encasing shale. The strong negative AVO trend is caused by the significant decrease in S-wave velocities of coal from overlying shale.

Figure 4.2-b shows the AVO trends of all lithologic units picked at Well C. It reveals that the zero-offset amplitude is controlled by P-wave velocity and density contrasts but the AVO by S-wave velocity contrast. The shale properties for the selected units are widely varying; P-wave velocity in 2700-3700 m/s, S-wave velocity in 1300-2000 m/s, and density in 2.3-2.6 g/cc. So the contrasts in rock properties between overlying shale and a reservoir unit are more decisive factors in AVO than individual reservoir unit's rock properties. Often shale properties are assumed to be almost constant and ignored in AVO analysis and interpretation, and that should be a non-trivial oversight.

Figure 4.3 shows AVO modeling results of three selected units (gas sand 2, wet sand 2, and coal 2) using different AVO equations; full Zoeppritz, Shuey (1985), Hilterman (1983), and Aki & Richard (1980). Other than full Zoeppritz equations, all approximations could be quite inaccurate for the incident angles larger than 10 degrees depending on lithologic models. For gas sands, all the approximations give almost the same reflection coefficients as full Zoeppritz equations up to 5° but for increasing incident angles, those values are getting more diverging. Sheuy's and Aki & Richard's approximations give almost the same computed reflection coefficients for all angle ranges as the full Zoeppritz equations. Hilterman's approximation gives the most divergent values. However, all the equations give the same positive AVO trend for all gas sands.

For wet sands, all the equations give almost the same reflection coefficients up to about 40°. For the angles greater than 40° Shuey's and Hilterman's approximations give a negative AVO trend but full Zoeppritz and Aki & Richard give a positive AVO trend.

For coal beds, all the equations give almost the same reflection coefficient values up to about 40°-incident angles, except those of Aki & Richard's approximation that show apparent differences for all incident angles. For incident angles above 40°,

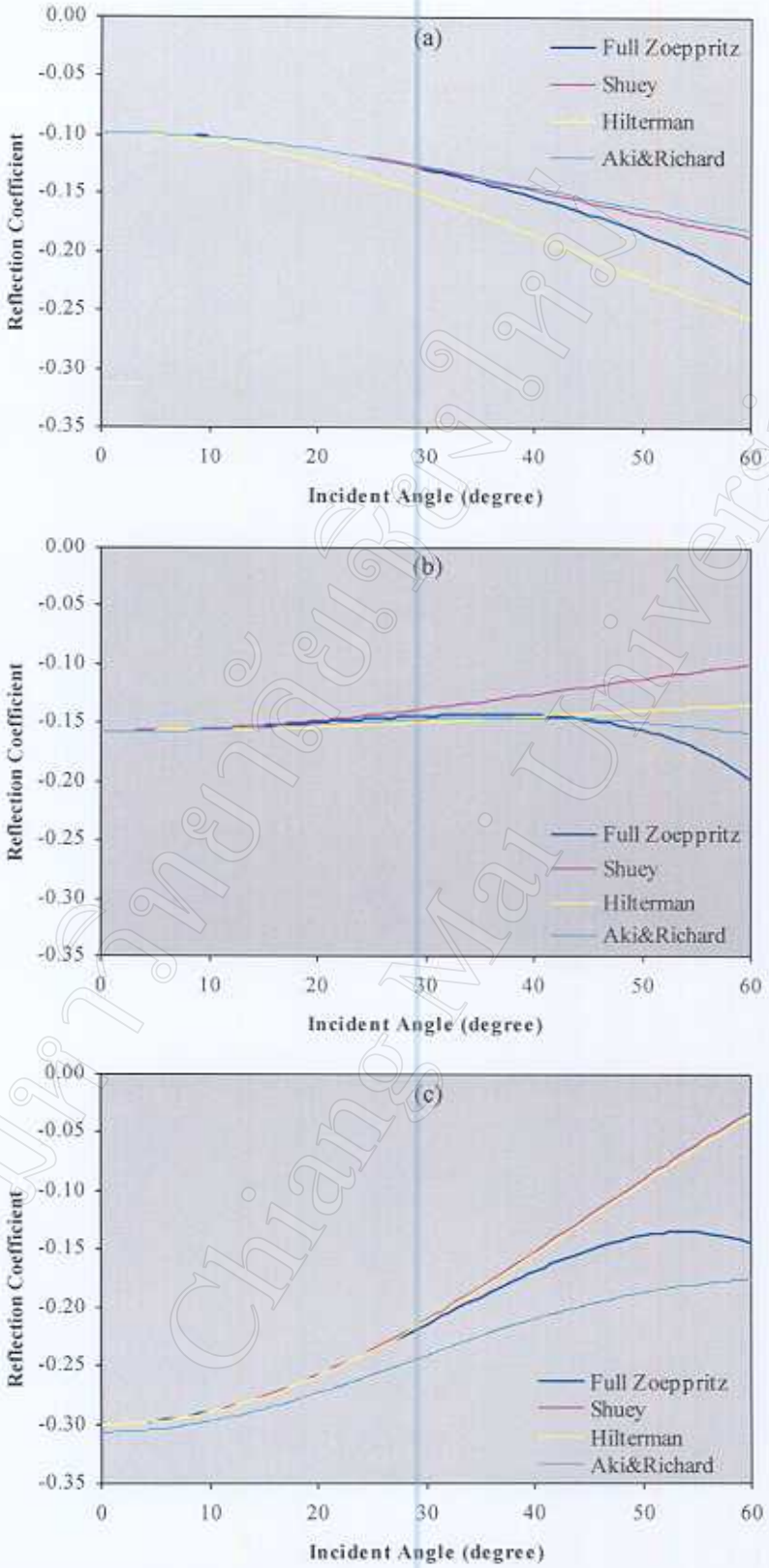

Figure 4.3 Reflection coefficient and incident angle relationships computed from the four Zoeppritz equations; for (a) the gas sand 2, (b) the wet sand 2 and (c) the coal bed 2.

ลิขสิทธิ์มหาวิทยาลัยเชียงใหม่
Chiang Mai University

Shuey and Hilterman reflection coefficients show almost the same values with negative AVO trends, but that of the full Zoeppritz show a negative AVO trend at incident angle up to about 55° and then give a positive trend at greater angles. Therefore, it is recommended to use the full Zoeppritz equations for AVO modeling and analysis.

4.2 Full elastodynamic modeling results

The Zoeppritz equations are limited to a single-boundary half-space modeling. For the modeling and evaluation of an entire geologic column with a suite of logs, the elastic wave equations should be solved. In this study, I used a computer software package developed by Youn (1998) for full elastodynamic modeling (solving 1st-order elastodynamic equations using a finite difference method).

Figure 4.4 shows a synthetic CDP gather generated by the elastodynamic-modeling program using the entire suite of sonic, density, and DSI logs from Well C. The top of valid logs is at 1110 m (1.1 sec per the VSP checkshot survey at the well). Figure 4.5 shows the same synthetic CDP gather from 0.9 sec to 1.9 sec. Figure 4.6 shows the same CDP gather after NMO corrections and mute (a milder mute than the surface seismic data because of an improved signal to noise ratio, S/N). These angle-bands are shown as before in the previous chapter, angle-band stacking, for comparison.

On the synthetic gather and real data, I was able to pick four gas sands (A, B, C, and D), four wet sands (A, B, C, and D), and three coal beds (A, B, and C). Many thin gas sands, wet sands, and coal failed to form independent and isolated events due to tuning and interference effects. The wet sands A, B, and C show strong amplitude levels with a flat AVO trend. The wet sand D shows a weak amplitude level with a negative AVO trend (actually it might be a flat trend but middle and far traces are contaminated with converted S-waves). The gas sand A shows a strong near-offset amplitude with a flat to slightly negative AVO trend. The gas sands B, C, and D show strong near-offset amplitude levels with a positive AVO trend. All the coal beds show strong to medium near-offset amplitude levels with a negative AVO trend.

The overall AVO variations of the picked units below 1.3 sec and in the far-offset range are affected by converted S-waves.

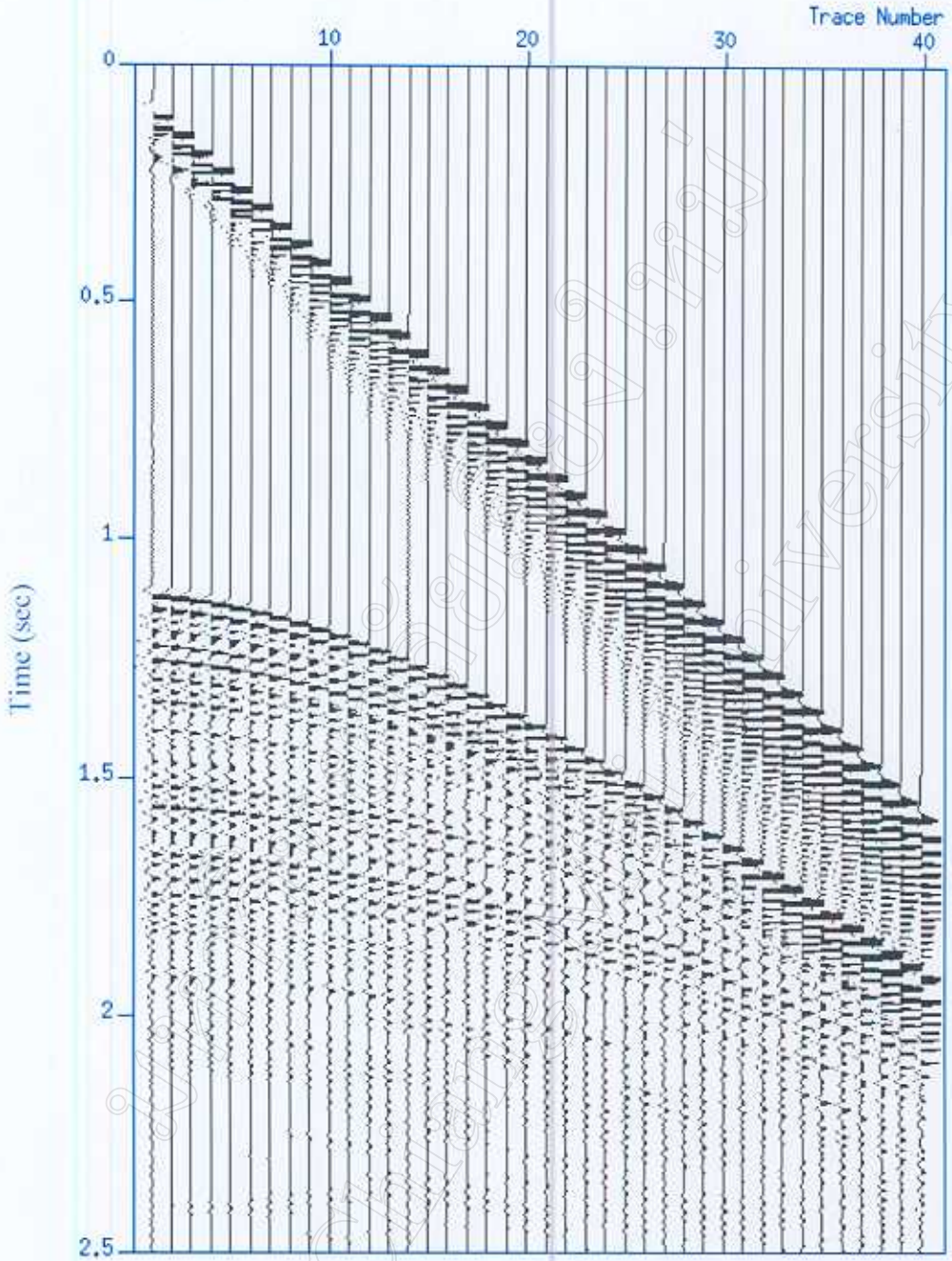

Figure 4.4 Synthetic CDP gather generated by the full elastodynamic modeling at Well-C.

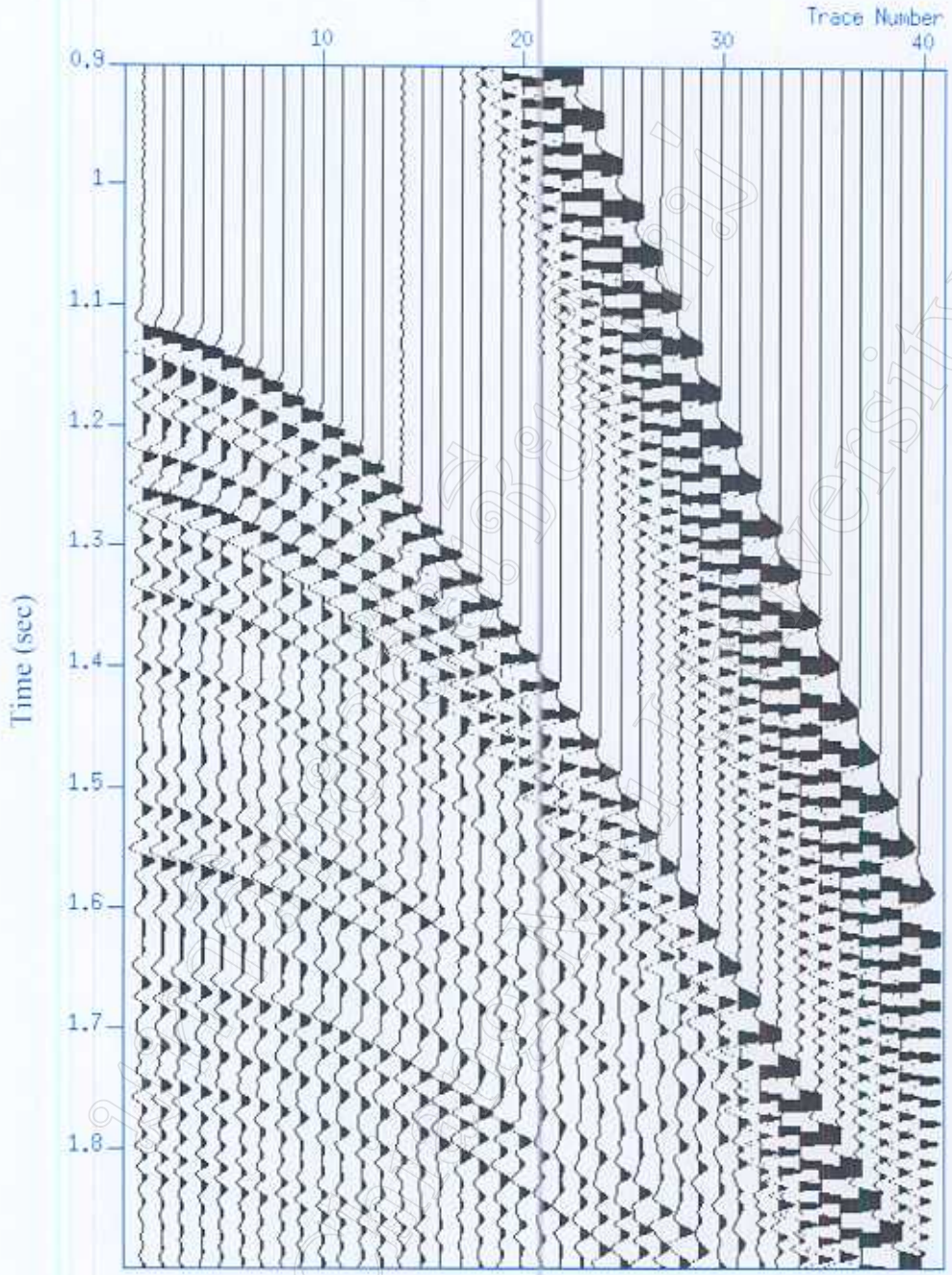

Figure 4.5 The same synthetic CDP gather shown in Figure 4.4 from 0.9 sec to 1.9 sec.

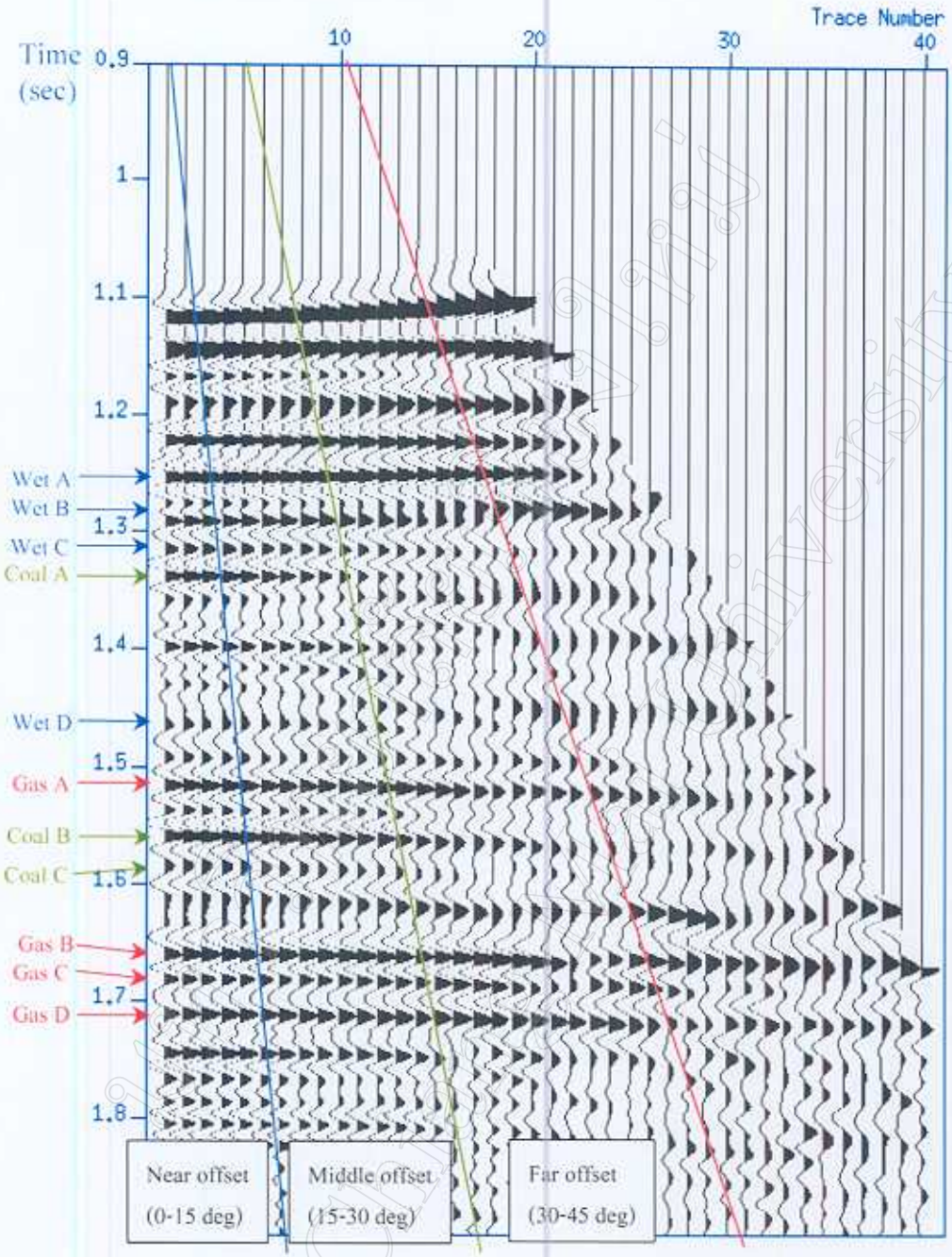

Figure 4.6 Final processed synthetic CDP gather at Well C.

4.3 Wavelet phase corrections for AVO analysis

The seismic wavelet phase is often confusing and uncertain, particularly for the correlation of synthetic with real data. To achieve a better correlation of the zero-phase synthetic CDP gather with the surface seismic CDP gather at the well location, I performed a phase-correlation-analysis program (a PTTEP software product) using the synthetic near trace and the real near trace from CDP 349 on line B (Figure 4.7). The program rotates the phase of real trace from –180 to +180 degrees at a 5-degree interval with simultaneous time shifts from –20 to +20 time samples for each rotation angle, and computes a cross-correlation value between two traces at each rotation and time shift, building a 2D matrix of correlation values. From this correlation matrix, an optimum phase-rotation angle and a time-shift amount are determined. After several tests and evaluations, I determined to rotate the real data by –180 degrees and to shift up 10 ms.. Figures 4.8 and 4.9 show the two CDP gathers (CDP 286 on line A and CDP 349 on line B) after the picked phase rotation and time shift. Seismic events picked from well C report and correlated with the synthetic model are shown on the left of the figures. Both gathers after phase rotation and time shift show improved correlation with the synthetic gather. Therefore, the subsequent AVO analysis used these phase rotated and time shifted real data.

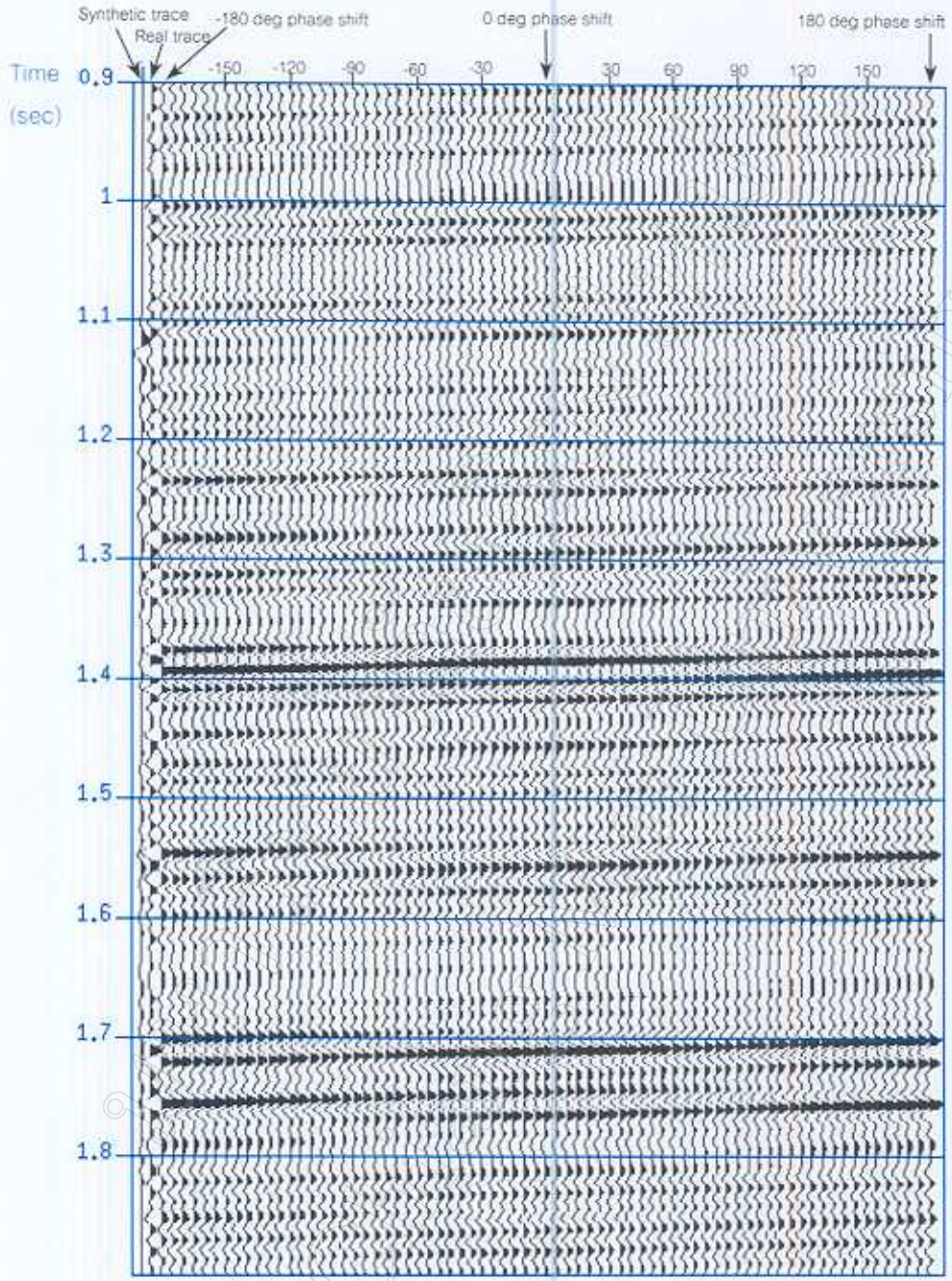

Figure 4.7 Phase correlation of two near traces, trace 1 from synthetic CDP and trace 2 from real CDP at Well C.

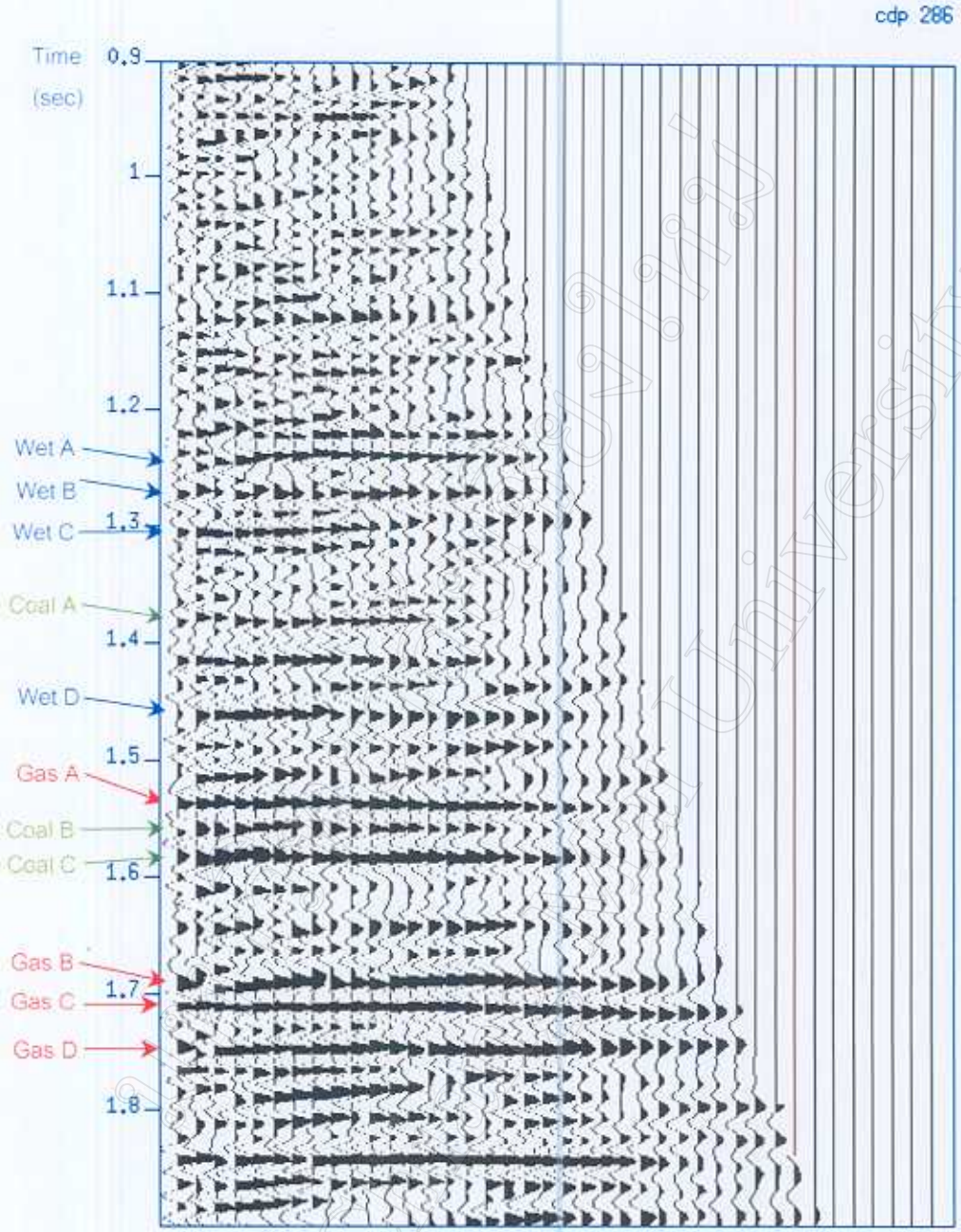

Figure 4.8 Processed CDP gather 286 on line A after phase rotation.

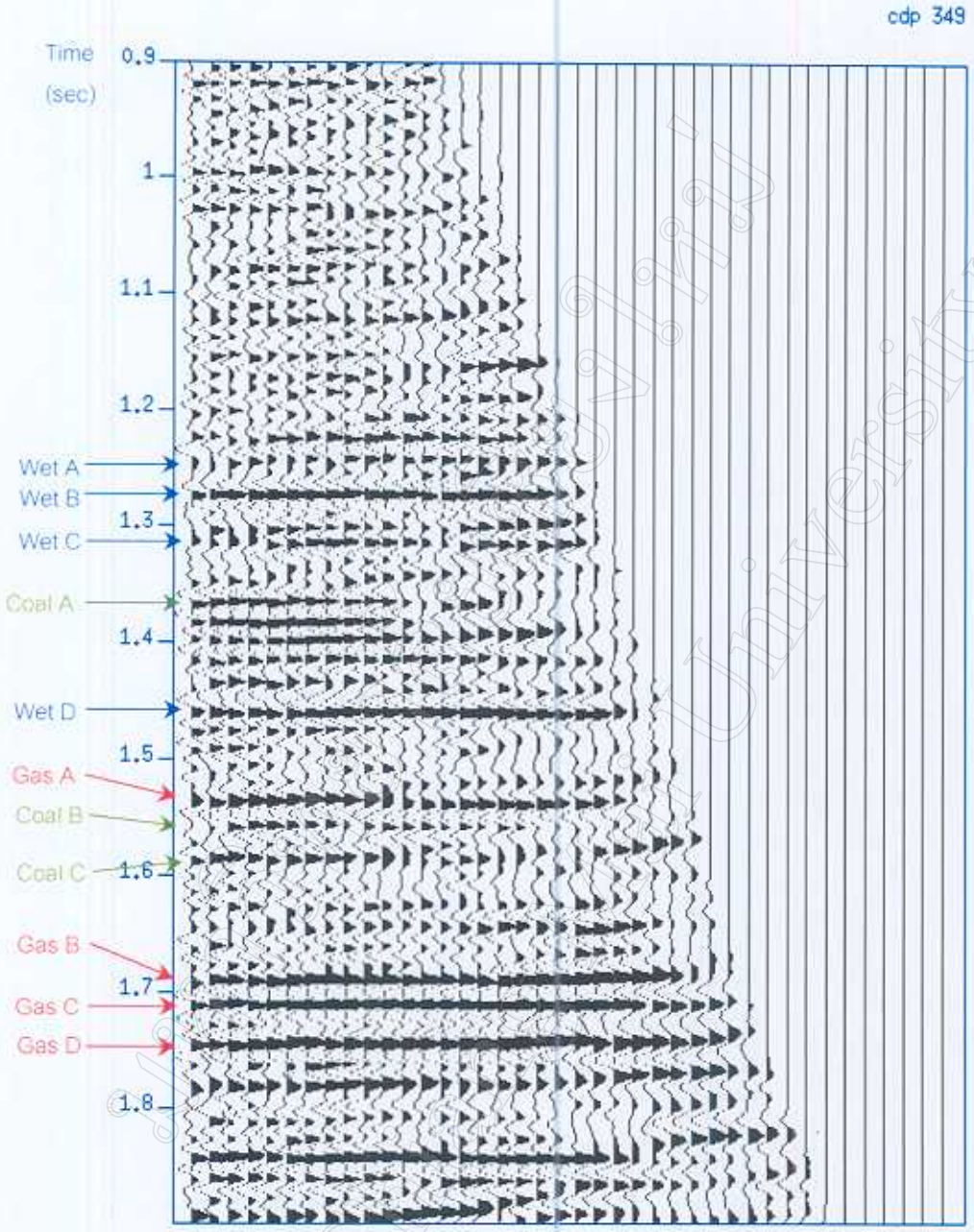

Figure 4.9 Processed CDP gather 349 on line B after phase rotation.